Nonvolatile Ferroelastic Strain from Flexoelectric Internal Bias Engineering

Wenhui Hou[®], ^{1,*} Shoieb A. Chowdhury[®], ² Aditya Dey[®], ² Carla Watson[®], ³ Tara Peña[®], ¹ Ahmad Azizimanesh[®], ¹ Hesam Askari[®], ² and Stephen M. Wu[®], ^{1,3,†}

¹Department of Electrical and Computer Engineering, University of Rochester, Rochester, New York 14627, USA

²Department of Mechanical Engineering, University of Rochester, Rochester, New York 14627, USA

³Department of Physics and Astronomy, University of Rochester, Rochester, New York 14627, USA

(Received 13 September 2021; accepted 14 January 2022; published 4 February 2022)

Internal bias in ferroelectric materials is a well-known phenomenon that offsets the ferroelectric polarization hysteresis loop along the electric-field axes. Control over this degree of freedom could lead to alternative classes of ferroelectric devices, as with control over the analogous concept of exchange bias in ferromagnetic devices. Currently, there lacks a systematic approach to engineering internal bias by design that allows for device-by-device control over this parameter, leading to difficulty in translating these concepts to the large-scale integration of ferroelectric electronics. In this work, the flexoelectric effect is used to engineer internal bias through the controlled deposition of stressed thin films onto ferroelectrics. Large strain gradients are generated near the surface of ferroelectric Pb(Mg_{1/3}Nb_{2/3})_{0.71}Ti_{0.29}O₃ single crystals through the deposition of stressed thin film strain gauges with increasing film force (film stress × film thickness). Using this technique, it is possible to continuously tune internal bias to control ferroelastic strain applied by the ferroelectric versus applied electric field, thereby achieving control of ferroelastic nonvolatility. Flexoelectric control of internal bias is verified by density functional theory and finite element analysis using a model with no free parameters, which matches both the expected magnitude and directionality of the flexoelectric field, and then further confirmed by piezoresponse force microscopy. This stress-induced flexoelectric effect utilizes popular strain engineering techniques already widely adopted by commercial complementary metal-oxide-semiconductor (CMOS) industrial fabrication processes, therefore sharing its advantages in scalability and reliability. Utilizing these techniques may lead to device-by-device level control of nonvolatility in ferroelectric field-effect or straintronic devices.

DOI: 10.1103/PhysRevApplied.17.024013

I. INTRODUCTION

Ferroelectric materials have numerous applications in electronic devices, such as ferroelectric randomaccess memories [1], ferroelectric field-effect transistors (FeFETs) [2], and ferroelectric tunnel junctions [3,4], attributed to their unique spontaneous polarizations, which are switchable under an applied electric field. Internal bias field [5] in ferroelectric materials is a well-known phenomenon that shifts the polarization-electric field hysteresis loop along the electric-field axes [Figs. 1(a) and 1(b)]. Like having full control of its counterpart in ferromagnetic materials, namely exchange bias [6,7], the ability to manipulate the internal bias field would add another degree of freedom in the engineering of ferroelectric materials and devices, with applications in areas such as logic devices and nonvolatile memories. There are various approaches to inducing internal bias fields, for example, through defect engineering [8–10], interface engineering [11,12], the flexoelectric effect [10,13,14], and so on. However, as multiple factors (composition and stoichiometry of the material, temperature, geometry of sample and electrodes, electrical loading characteristics, etc.) are involved, fully understanding and manipulating internal bias is still challenging. Furthermore, since most of current techniques to manipulate internal bias are changes made to global variables or conducted through applied external forces, the idea of using these various concepts to individually tune the internal bias in individual electronic devices on a single chip is challenging. Since this is a prerequisite for the large-scale integration of scalable ferroelectric devices with individually continuously tunable internal biases, it is an important milestone to be able to achieve the same level of manufacturability (approximately 10¹² transistors per chip) as the current complementary metal-oxide-semiconductor (CMOS) processes.

One other commonly used application of ferroelectrics is to apply ferroelastic strain to other materials through the converse piezoelectric effect (straintronics). This method

^{*}whou4@ur.rochester.edu

[†]stephen.wu@rochester.edu

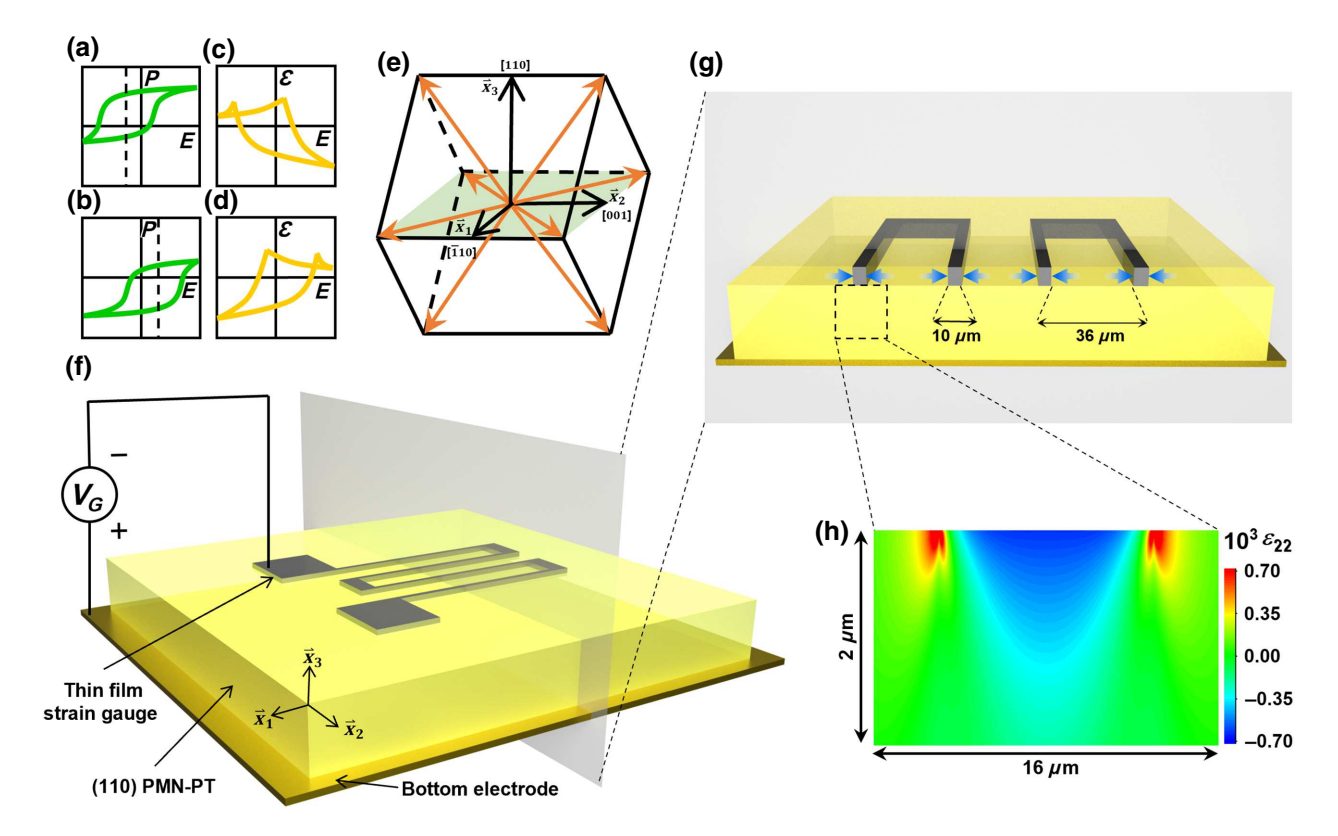


FIG. 1. (a) and (b) Ferroelectric polarization hysteresis curves with positive internal bias field and negative internal bias field, respectively. (c) and (d) Ferroelastic strain responses correspond to (a) and (b). (e) Rhombohedral unit cell with eight possible (111) polarization variants of the PMN-PT substrate. (f) Schematic of the device configuration. (g) Schematic of a cross section of the device, where blue arrows represent the film force. (h) A typical strain distribution in the PMN-PT substrate underneath the metal strip.

of introducing strain has its unique advantages compared with other approaches, such as through lattice mismatch [15] or bending a flexible substrate [16], as it provides an electric-field controllable strain. Using ferroelastic strain, previous works have successfully demonstrated modification of strain-sensitive material properties, such as magnetization, resistivity, and ferromagnetic resonance of thin films (FeRh [17,18], Co₄₀Fe₄₀B₂₀ [19], Co [20], Fe₂O₃ [21], Fe₆₀Co₂₀B₂₀ [22], etc), or even completely switching between electronic phases of exfoliated two-dimensional (2D) materials [23] on top of a ferroelectric substrate. One main feature of ferroelastic strain is that the strainelectric field (ε –E) response is a symmetric, butterflylike curve without remanent strain, i.e., it is volatile. However, for the purpose of nonvolatile memory [24], asymmetric nonvolatile strain is more desirable in strain-based information storage devices. This can be achieved by breaking the symmetry either externally through asymmetric electric-field sweeping [21,22,25] or internally through introducing an internal bias field [26]. Because of the correlation between ferroelectric polarization and ferroelastic strain, when the polarization hysteresis loop is offset by the internal bias along the electric-field axis, the corresponding ferroelastic strain curve will also deviate from the symmetric butterflylike curve and show asymmetric and nonvolatile behavior, as shown in Figs. 1(c) and 1(d). Other approaches, such as through a controlled polarization switching path (109° ferroelastic switching) in a specific orientation of the ferroelectric crystal [19] or electric-field-induced irreversible phase transitions of ferroelectrics [27], have also been demonstrated to introduce nonvolatility into ferroelastic strain. However, there is a lack of a scalable method to achieve continuous engineerable control over ferroelastic nonvolatility that is compatible with the large-scale integration of devices that has the same degree of sophistication as modern CMOS manufacturing techniques.

In this work, we show that by using controlled deposition of stressed thin films onto ferroelectric materials, we can control the internal bias through the flexoelectric effect [28,29], and in turn achieve control over the nonvolatile application of ferroelastic strain. Strain engineering with stressed thin films has an almost 20-year history in commercial CMOS integrated circuit manufacturing and has been intensively modeled and verified by process simulation with finite element analysis (FEA) [30]. With the deposition of a stressed thin film layer, typically silicon nitride, onto the transistor, strain can be introduced

into the channel through stress transfer and be used to enhance electron or hole mobility [31–33]. This type of process-induced strain engineering is so widely used that almost all electronics since the 90 nm technology node in 2004 have utilized this concept to some degree [30]. By adopting a similar approach, we deposit stressed thin films on top of ferroelectric substrates to engineer nonuniform strain into the ferroelectric lattice. With a compressive (tensile) film stress, the substrate expands (contracts) locally near the interface owing to the presence of the stressor, resulting in strain gradients in the ferroelectric lattice. Due to the flexoelectric effect, which is the coupling between polarization and strain gradients, a positive (negative) internal bias is present in the ferroelectric material, which offsets the polarization-electric field hysteresis loop to the left (right), as shown in Fig. 1(a) [Fig. 1(b)]. Because of the correlation between strain and polarization, the ferroelastic strain response also deviates from the symmetric butterflylike curve and shows an asymmetric nonvolatile behavior [Figs. 1(c) and 1(d)]. Since the strain gradients are directly proportional to controllable quantities like film stress, we also demonstrate a continuous tuning of the flexoelectric effect, enabling fine control of nonvolatility in ferroelastic strain. Past approaches, such as lattice mismatch [14,34] or inducing strain gradients using atomic force microscope (AFM) probes [35–38], have made significant strides for controlling the nanoscale flexoelectric effect. The unique advantage with our approach of implementing the flexoelectric effect is that it shares the advantages of scalability and reliability with longestablished strain engineering techniques, which can be directly translated into current semiconductor manufacturing processes at the device-by-device level. Therefore, these techniques can be applied to ferroelectric or straintronic devices individually with direct control over internal bias magnitude and direction for each device, much like compression and tension is controlled in strained silicon technology to enhance hole or electron mobility depending on whether transistors are p-channel (PMOS) or n-channel (NMOS). These concepts, therefore, may have immediate benefits to converse piezoelectric-effect-based straintronic applications [17–23], and the recent renaissance of deeply scaled FeFET devices [39,40], where device-level tuning of internal bias may allow for more exciting logic or memory functionality.

II. DEVICE CONFIGURATION

To test our concept, we use a (110)-oriented relaxor ferroelectric $Pb(Mg_{1/3}Nb_{2/3})_{0.71}Ti_{0.29}O_3$ (PMN-PT) single crystal as the substrate, which has been reported to have both a large in-plane (IP) converse piezoelectric strain response [25] and large flexoelectric effects [41,42]. Figure 1(e) shows its rhombohedral unit cell with the eight possible domain variants with (111) oriented polarizations.

The four domain variants with IP polarizations show high remanent IP strain whereas the other four domain variants with out-of-plane (OP) polarizations show low remanent IP strain [21,25]. On top of this ferroelectric substrate, we micropattern strain gauges made from electron-beam (e-beam) evaporated metal thin films with various film stresses. The device configurations are shown in Fig. 1(f). By poling the ferroelectric substrate with a gate voltage V_G across the PMN-PT and measuring the resistance change of the strain gauges, we are able to quantify the average IP converse piezoelectric strain response of the domains underneath the gauge. Here, the resistance changes ΔR , $\Delta R = R - R_0$, where R_0 and R are the resistance of the strain gauge at $V_G = 0$ and under a poling voltage V_G , respectively, are converted into strain responses through the equation $\varepsilon = (\Delta R/R_0)/GF$, where ε is the IP strain, and GF is the gauge factor. In Appendix A, we explain how the gauge factor is measured in detail. Each strain gauge consists of four 480- μ m-long metal strips with other dimensions shown in Fig. 1(g). As there is always a certain amount of intrinsic film stress in an e-beam evaporated metal thin film [43], depending on whether it has tensile or compressive stress, the film tends to contract or expand to relax the stress. However, as the film is bonded on the substrate and does not uniformly cover the whole substrate, this results in a nonuniform strain distribution (strain gradient) both inside the thin film and the underlying substrate. Film force, F_f , $(F_f = t_f \bar{\sigma})$, where $\bar{\sigma}$ is the average film stress and t_f is the film thickness), is used to quantify the applied force onto the PMN-PT substrate. By convention, positive values are assigned to tensile film forces and negative values to compressive forces. Details for the measurement of film force are shown in Appendix A. Figure 1(h) shows a typical strain distribution inside the PMN-PT substrate underneath a metal strip with tensile film stress obtained by our FEA. Thus, by using the metal thin film strain gauges, we are able to introduce a nonuniform strain distribution (strain gradient) inside the ferroelectric crystal and measure the corresponding converse piezoelectric strain response at the same time.

III. RESULTS AND DISCUSSION

A. Strain response with respect to film stress

To vary the film stress while keeping the same interface between the metal thin film and PMN-PT substrate, we fabricate strain gauges made from a 50-nm Ag thin film and a 50-nm Cr thin film on top of a 25-nm Ag thin film (Ag/Cr bilayer film). Here, silver, as a low melting point metal with high surface mobility, exhibits low tensile film stress, whereas chromium, as a high melting point metal with low surface mobility, exhibits high tensile film stress [43,44]. The film force for the silver-only film is measured to be 3.6 N m⁻¹ and the film force for

the Ag/Cr bilayer film is measured to be 27.8 N m⁻¹. Since silver is more conductive than chromium (the resistance of the 25-nm Ag layer is measured to be around 200 Ω , whereas the resistance of the 50-nm Cr layer is measured to be around 1600 Ω), current mostly flows through the Ag layer, which makes both the silver-only and the Ag/Cr bilayer film strain gauges have similar gauge factors (7.7 and 7.1, respectively). Figure 2(a) shows a typical IP strain response of the PMN-PT under the silver-only strain gauge, which is nonvolatile and unipolar with a left-hand polarity (shows high remanent strain after applying a negative gate voltage), similar to the strain response of Fig. 1(c). Figure 2(b) shows a typical IP strain response of the PMN-PT under the Ag/Cr bilayer film strain gauge, which is also nonvolatile and unipolar, but with a right-hand polarity (shows high remanent strain after applying a positive gate voltage), similar to the strain response of Fig. 1(d). Results similar to those in Figs. 2(a) and 2(b) are confirmed by 15 silver-only strain gauges and 10 Ag/Cr bilayer strain gauges on various PMN-PT substrates containing the same intrinsic internal bias field (PMN-PT crystals cut from same batch). The qualitative explanations for the opposite strain responses are given in Figs. 2(c) and 2(d), respectively. For the silver-only strain gauges with low film force, the nonuniform strain in the PMN-PT underneath the metal strip is small, thus the flexoelectric-effect-induced internal bias is trivially small. The left-hand unipolar nonvolatile strain is caused by the positive intrinsic internal bias of the PMN-PT substrate, as shown in Fig. 2(c). Intrinsic internal bias has been widely observed in ferroelectric single crystals in their as-grown state, which can result from defect dipole alignment during

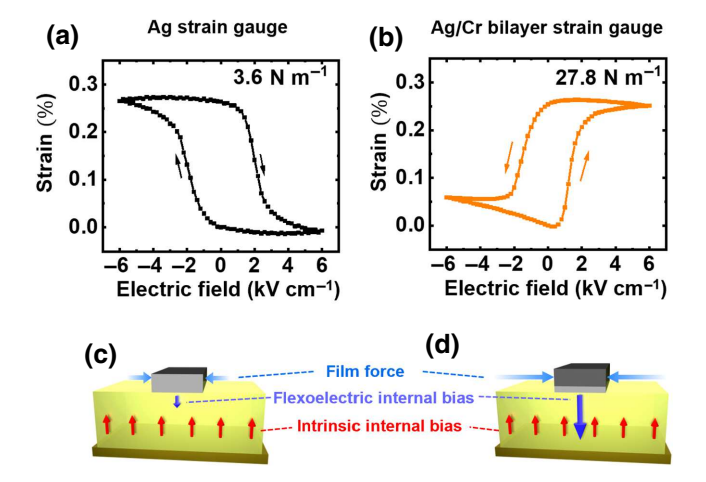


FIG. 2. (a) Strain response of the PMN-PT substrate underneath the Ag-only film with a film force of 3.6 N m⁻¹. (b) Strain response of the PMN-PT substrate underneath the Ag/Cr bilayer film with a film force of 27.8 N m⁻¹. (c) and (d) Schematic of the intrinsic internal bias and the flexoelectric effect induced internal bias in the PMN-PT substrate underneath the Ag-only film and the Ag/Cr bilayer film, respectively.

the crystal growth process [5,45,46]. However, for the Ag/Cr bilayer film strain gauges with high film force, the nonuniform strain in the PMN-PT is large. This causes a strong negative flexoelectric internal bias which surpasses the positive intrinsic internal bias, thus resulting in the unipolar nonvolatile strain response with opposite polarity, as shown in Fig. 2(d). It is worth mentioning that the results observed here cannot be explained by the bias field caused by the asymmetric bottom and top electrodes as silver is the contact material with PMN-PT for the top electrode in both cases, and more generally, the work function difference between the top and bottom electrode is of the order of 1 V, whereas we are applying a 150 V gate voltage across the bulk PMN-PT single crystal. The results also cannot be explained by the change of the charge screening efficiency in the silver and PMN-PT interface, since the thicknesses of the metal thin films we use are well above the typical charge screening length for simple metals, which is of the order of an angstrom [47].

To further investigate the transition of the strain response from the left-hand unipolar curve to the righthand unipolar curve, we gradually increase the applied film force to evaluate how the strain response changes correspondingly. To do this, we deposit different thickness of nickel on top of a 25-nm silver film (Ag/Ni bilayer film). As the melting point of Ni is higher than silver and lower than chromium, the average film stress $\bar{\sigma}$ of evaporated Ni thin films is also in between those of evaporated Ag thin films and Cr thin films [48]. Therefore, by gradually increasing the thickness of the evaporated Ni layer, we are able to control the film force F_f ($F_f = t_f \bar{\sigma}$) of the Ag/Ni bilayer film to increase from a film force close to that of the Ag-only film to a film force close to that of the Ag/Cr bilayer film, as shown in Fig. 3(a). Based on this, we fabricate Ag/Ni bilayer film strain gauges made from 25-nm, 40-nm, 55-nm, and 70-nm Ni on top of 25-nm Ag, which are measured to result in film forces of 8.1, 13.0, 18.6, and 22.5 N m⁻¹, respectively. Again, since silver is more conductive than nickel (the resistance of 25-70-nm Ni layers is measured to be in the range 600–1600 Ω), current mostly flows through the Ag layer (by a factor of 3 to 8 times). Figures 3(b)-3(e) show the corresponding IP strain responses of the PMN-PT measured from these strain gauges. As the film force increases from left to right, a gradual transformation from the left-hand unipolar nonvolatile curve [Fig. 3(b)] to the right-hand unipolar nonvolatile curve [Fig. 3(e)] can be seen, with a bipolar volatile curve in between [Fig. 3(c)]; this indicates that the positive intrinsic internal bias of the PMN-PT substrate is gradually overcome by the negative internal bias induced from the flexoelectric effect. The strain responses we measure from the three kinds of strain gauges (Ag-only, Ag/Cr bilayer, Ag/Ni bilayer) in Figs. 2 and 3 are comparable because the Ag is always the layer in contact (same interface between the strain gauges and the PMN-PT substrate), and the

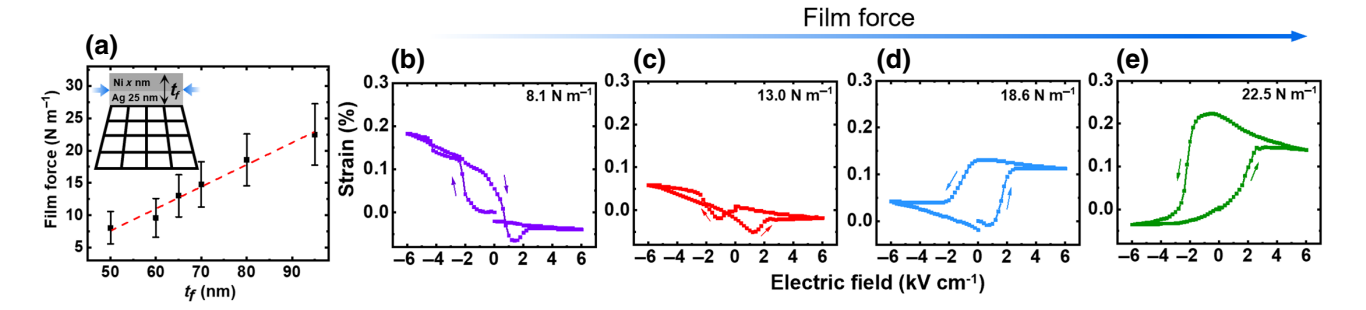


FIG. 3. (a) Film force of the Ag/Ni bilayer film as a function of the film thickness. Inset shows schematic of the Ag/Ni bilayer film on top of the deformed lattice of the substrate. Blue arrows represent the film force. (b)–(e) Strain response of the PMN-PT substrate underneath the Ag/Ni bilayer film with a film force of 8.1, 13.0, 18.6, and 22.5 N m⁻¹, respectively.

current always mostly flows through the Ag layer. The similar shape of the strain responses from Figs. 2(b) and 3(e) also verifies that this effect is not because of the composition of the strain gauges, but mainly due to the film force of the strain gauges. Within these sets of experiments, it is demonstrated that we have continuous engineerable control over ferroelastic nonvolatility in our devices.

B. Modeling of the flexoelectric effect

To quantify the flexoelectric effect, we perform FEA of the strain distribution in the PMN-PT induced by the Ag/Cr bilayer film stressor consisting of 50-nm Cr on top of 25nm Ag. The FEA methods used here have a long-standing history in process simulation for strained commercial silicon-based transistors and have been used exclusively to model strain in Si since the inception of strain engineering as a concept. We seek to use these same methods to understand strain gradients in our ferroelectrics, while reconfirming with local experimental probes (Sec. C). Here, the Ag/PMN-PT interface is described by a surface-based cohesive law with linear traction-separation behavior in the FEA model and characterized by a constant interfacial shear modulus G_{int} . This is necessary to model imperfect bonding at the Ag and PMN-PT interface and represents the interface as a more compliant layer in between the two constituent materials, typical for systems of thin film metals on oxides. The value of $G_{\rm int}$ is determined to be 3.6 GPa through density functional theory (DFT) calculation and compared with other previously reported interfacial shear modulus values of various metal-dielectric interfaces in Appendix B (Table I). Owing to the high length-to-width ratio of the strips, the strain components corresponding to the length direction would be nearly uniform at any location along the strips. Consequently, those strain gradients and their contribution to flexoelectric polarization would be orders of magnitude smaller. Hence, the plane-strain assumption is used in FEA to model the strain distribution in the $\vec{x}_2\vec{x}_3$ plane [same coordinates as in Figs. 1(e) and 1(f)]. The details of the FEA and DFT simulation can be found in Appendix C.

Figures 4(a)-4(c) show the simulated strain distributions inside the PMN-PT underneath the Ag/Cr bilayer film, where ε_{22} and ε_{33} describe the normal strain in the IP (\vec{x}_2) and the OP (\vec{x}_3) directions, respectively, and ε_{23} describes the shear strain in the $\vec{x}_2\vec{x}_3$ plane. As shown in Figs. 4(a) and 4(b), there are large strain gradients formed inside the PMN-PT underneath the stressor layers near the surface region (approximately 1 μ m in depth). It is important to note that the normal strains ε_{22} and ε_{33} shown in Figs. 4(a) and 4(b) are axially symmetric, while the shear strain ε_{23} shown in Fig. 4(c) is antisymmetric across the strip. Based on the simulated strain distribution results in Figs. 4(a)-4(c), we calculate the corresponding flexoelectric field near the surface of the PMN-PT (1 μ m in depth) with the details of the calculation described in Appendix C. As shown in Fig. 4(d), the average magnitude of the flexoelectric field close to the surface of the PMN-PT underneath the strip is around 2.6 kV cm⁻¹, which is 1 kV cm⁻¹ higher than the coercive field of PMN-PT (approximately 1.6 kV cm⁻¹) [25]. The direction of the flexoelectric field in the OP direction is pointing downward, thus causing a strong negative internal bias in the PMN-PT. This matches with the prediction in Fig. 2(d). Moreover, the FEA results also reveal the unique asymmetry resulting from the effect of the antisymmetric shear strain ε_{23} on the flexoelectric field in the IP direction (\vec{x}_2) . Under the strip, \overline{E}_{flexo} is pointing to the right ([001]) for the left portion whereas $\overline{E}_{\text{flexo}}$ is pointing to the left ([00 $\overline{1}$]) for the right portion, with the former region slightly wider than the latter, as marked by the black dashed line. This asymmetry could only arise due to the shear component of the flexoelectric effect, and is experimentally probed for as further evidence for flexoelectric induced internal bias modification in the following section (Sec. C). Additionally, as we traverse from left to right in the entire modeled region of the ferroelectric substrate, we see that the IP domain configuration due to the flexoelectric field should have a "left-right-left-right" configuration, which is also probed for experimentally as verification of our simulation.

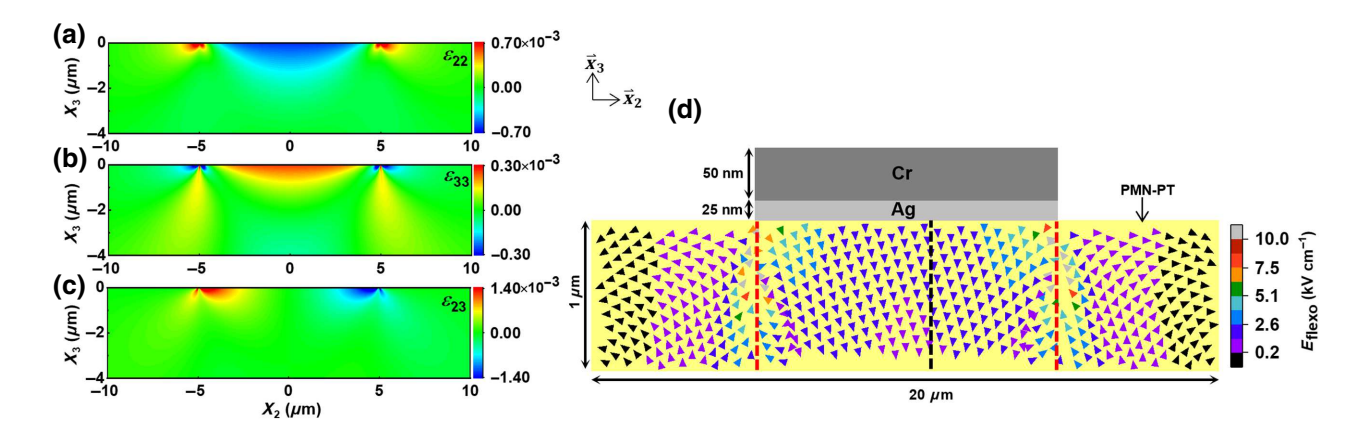


FIG. 4. (a)–(c) FEA simulations of the normal strain ε_{22} and ε_{33} , and shear strain ε_{23} distributions inside the PMN-PT underneath the Ag/Cr bilayer film. (d) Calculated flexoelectric field ($E_{\rm flexo}$) distribution inside the PMN-PT based on the simulation results of (a), (b) and (c). Here, the direction and the color of each arrow represent the direction and the magnitude of $E_{\rm flexo}$, respectively. The red dashed lines show the locations of the edges of the Ag/Cr bilayer film. The black dashed line shows where the IP component of $E_{\rm flexo}$ reverses direction.

C. Verification of modeling results by piezoresponse force microscopy (PFM)

PFM is a well-known method used to map surface domains in ferroelectrics, and can sense surface domains up to approximately 1 μ m in depth [49]. This depth resolution matches with the length scale of the flexoelectric field predicted in Fig. 4. Furthermore, according to the modeling results (Sec. B), the flexoelectric field results in a unique surface domain configuration in the PMN-PT along the IP direction. Therefore, we use PFM to systematically investigate the surface domain patterns of the PMN-PT substrate after the electrical measurements of the strain gauges to serve as further verification of the FEA model. We choose the Ag/Cr bilayer film strain gauges as they show the strongest right-hand nonvolatile unipolar strain response resulting from the flexoelectric effect. Figure 5(a) shows a typical Ag/Cr bilayer film strain gauge and the corresponding strain response. The poling sequence of the last electric-field sweeping is $0 \rightarrow +6 \rightarrow 0 \rightarrow -6 \rightarrow 0 \text{ kV cm}^{-1}$ between the bottom electrode and the strain gauge. With the right-hand polarity of the strain response, the part of the PMN-PT substrate underneath the metal strip is therefore left at the low remanent strain state, which corresponds to the domain states with downward OP polarizations. The strain gauges are then removed by a relief polishing process with details described in Appendix A. Because domains with downward polarizations have a lower abrasion rate than ones with upward polarizations [50], the surface domain structures are revealed after the relief polishing. Multiple works have already demonstrated that through relief polishing, the topographic image will show the ferroelectric domain structure without changing the domain orientation itself [50–54]. As shown in Fig. 5(b), the region that had been underneath the strain gauge with downward polarizations appears to be smooth and higher than the surrounding regions, whereas the region far away from the former appears to be uneven with a mottled pattern [50] because of the annealing process before device fabrication, which sets the polarizations pointing randomly along the eight possible (111) directions. This also shows that the built-in intrinsic internal bias field is not large enough to reorient the polarizations in the PMN-PT by itself.

PFM measurements are then conducted over an area that covers both the region that had been underneath the metal strip and the regions next to it less than an hour after the removal of the stressor layers. It has already been demonstrated by multiple works that the domain patterns set by the flexoelectric effect are relatively stable and show no relaxation for over 12 h to several days after the removal of the applied force that induced the flexoelectric field [35,38,55]. To uniquely identify the polarization direction for each domain, we perform one vertical (V) PFM [Fig. 5(c)] and two lateral (L) PFM measurements with the AFM probe along [001] [Fig. 5(d)] and $[\bar{1}10]$ [Fig. 5(e)], respectively, where the VPFM can image the OP polarization component and the LPFM can image the IP component perpendicular to the AFM probe. Figure 5(c) shows the VPFM phase image. Here, the measurement is sensitive to polarizations with an OP component, which are represented by the four polarization vectors in Fig. 5(f). Thus, the dark region indicates downward polarizations with two possible variants [marked as the blue and purple vectors at the bottom of Fig. 5(c) and in 5(f)] whereas the bright region indicates upward polarizations with the other two possible variants [marked as green and yellow vectors at the bottom of Figs. 5(c) and 5(f)]. Figure 5(d) shows the LPFM phase image with the AFM probe along [001]. Here, the measurement is sensitive to polarizations that have an IP component perpendicular to [001], which are

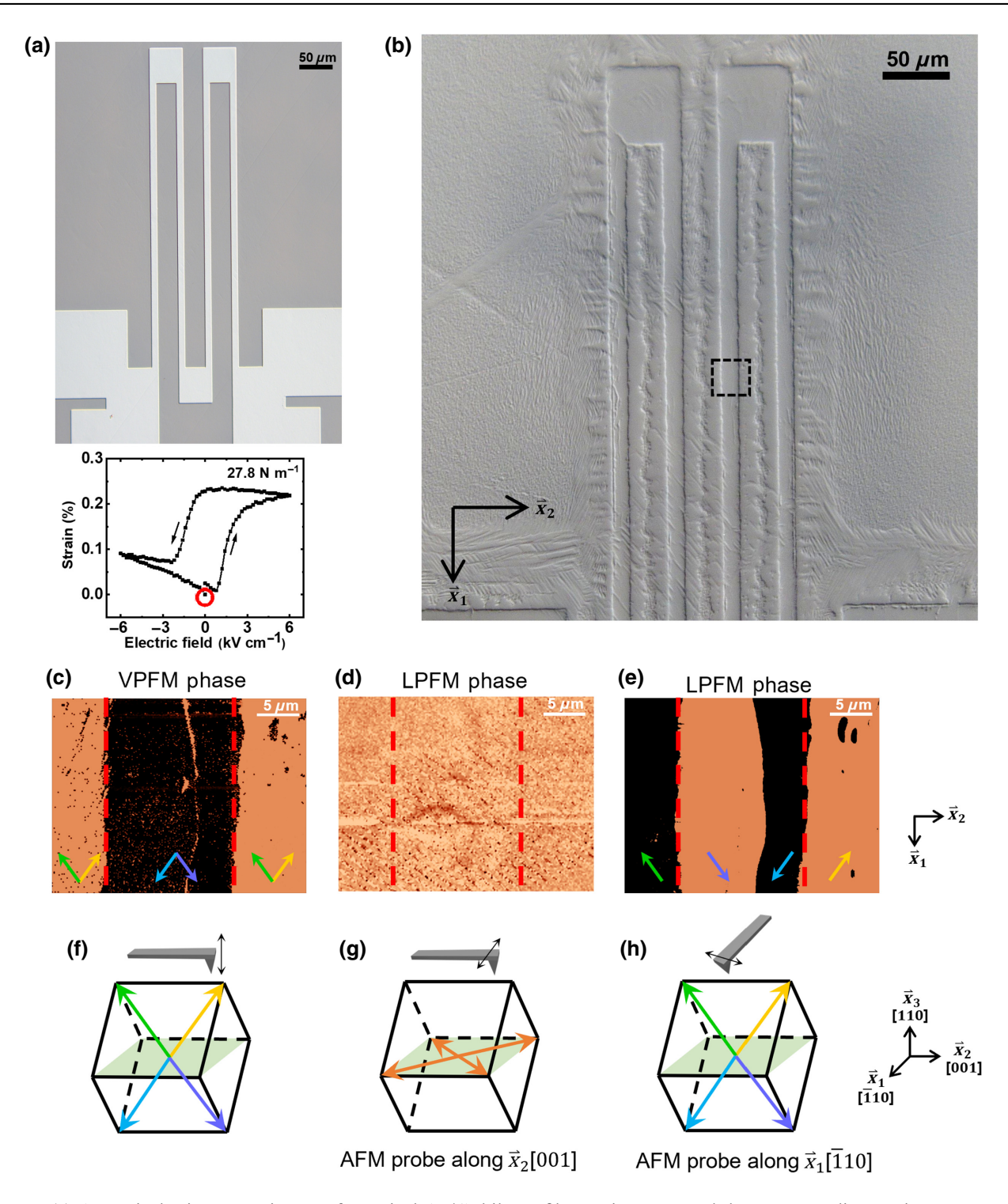


FIG. 5. (a) An optical microscope image of a typical Ag/Cr bilayer film strain gauge and the corresponding strain response. Red circle marks the strain state the device is left in after the electric-field cycling. (b) An enlarged version of (a) after the relief polishing process under the optical microscope with differential interference contrast. Dashed square marks the region where the PFM is conducted. (c)–(e) VPFM, LPFM (AFM probe along [001]), and LPFM (AFM probe along [101]) phase images. The two red dashed lines show the region that had been covered by the metal strip. Colorful arrows at the bottom indicate possible polarization vectors that can result in the corresponding phase result. (f)–(h) Schematics of the polarization vectors that the measurements in (c)–(e) are sensitive to with the corresponding probe orientation and vibration mode (marked by the black double-headed arrow) for each PFM measurement, respectively.

represented by the four polarization vectors in Fig. 5(g). However, no contrast is seen in Fig. 5(d), which indicates that there are no IP polarizations in the scanned area. Figure 5(e) shows the LPFM phase image with the AFM probe along $[\bar{1}10]$. This time, the measurement is sensitive to polarizations which have an IP component perpendicular to [110]. Although all eight polarization directions along (111) have IP components perpendicular to [110], using the result from Fig. 5(d), we can eliminate four variants. Only the vectors shown in Fig. 5(h) may cause contrast in Fig. 5(e). Therefore, by combining all three PFM results, the polarization direction for each domain can be uniquely identified, as marked at the bottom of Fig. 5(e). Here, the OP directions of the measured domains are the combined results determined from the applied external electric field, intrinsic internal bias field, and the flexoelectric field, whereas the IP directions of the domains are solely determined from the flexoelectric field, which perfectly matches the left-right-left-right configuration modeled for the flexoelectric field [Fig. 4(d)]. Moreover, the asymmetry of the polarization in the IP direction of the PMN-PT underneath the strip predicted in Fig. 4(d) is also observed in the PFM result in Fig. 5(e), where the brighter region between the two red dashed lines is slightly wider than the darker region between the two red dashed lines. This effect is reproduced in multiple regions of the strain gauge presented in Fig. 5, as well as other separate strain gauges with other film force magnitudes. This asymmetry exactly matching our FEA simulations, which has no free parameters in its model, provides further direct confirmation that the effects we observe in the control of nonvolatile strain arise from flexoelectric-induced internal bias modifications to the surface of the PMN-PT. It is worth mentioning at this point that all the methods we introduce here are surface sensitive effects, since the flexoelectric effects are limited to the surface (approximately 1 μ m in depth) of the PMN-PT substrate. The gauges only measure strain applied by the domains directly underneath itself at the surface, while PFM only probes surface polarizations (approximately 1 μ m in depth) of the PMN-PT single crystal. Direct polarization versus electric-field measurements would likely not elicit the same effect since our PMN-PT substrates are 0.25 mm in thickness, whereas it is likely that in thin film ferroelectrics there could be a directly measurable effect, which can be done by using the recently reported ferroelectric membranes that are free from substrate clamping [56–58].

IV. CONCLUSION

We introduce another approach to induce the flexoelectric effect in ferroelectric materials, by which controllable internal bias and polarity reversibility of nonvolatile ferroelastic strain can be achieved. This method differs from flexoelectric control reported in the past because it uses

techniques that have device-by-device continuous control of strain that have long been used in commercial fabrication processes in densely integrated and aggressively scaled transistor technology. Flexoelectricity is verified through process simulation with FEA using a model with no free parameters, which exactly matches the expected magnitude of the flexoelectric field, directionality of flexoelectric polarization, and shear flexoelectric asymmetry. This provides a path to realize nonvolatile control of strain sensitive materials properties (resistivity, band gap, magnetization, ferromagnetic resonance, superconductivity, etc.) in deposited thin films and 2D materials in ferroelastic-strain-based (straintronic) devices [17–23]. In fact, in many previously reported works on magnetic thin films on PMN-PT, there is always a small degree of straintronic nonvolatility associated with asymmetry with respect to electric-field sweeping that may be due to unaccounted for strain-induced flexoelectric effects. With our acquired knowledge and the ability to engineer the polarity of strain nonvolatility, both PMOS-like and NMOSlike nonvolatile straintronic devices may potentially be explored using the same base material as a channel, which is difficult to obtain using ferroelectric field effect alone [40]. The ability to control internal bias also benefits ferroelectric field-effect-based electronic devices by adding another degree of freedom in those applications, especially in engineering ultrathin scalable ferroelectrics such as Hf_{0.8}Zr_{0.2}O₂ with CMOS compatibility [39,40]. By adapting a long-established technique from the semiconductor industry, i.e., stressed capping layer-based strain engineering [31–33], the thin film stress-induced flexoelectric effect we demonstrate here may lead to a scalable method to control nonvolatile FeFETs or straintronic devices.

ACKNOWLEDGMENTS

We wish to acknowledge support from the National Science Foundation (Grants No. OMA-1936250 and No. ECCS-1942815) and the National Science Foundation Graduate Research Fellowship Program (Grant No. DGE-1939268).

APPENDIX A: EXPERIMENTAL DETAILS

PMN-PT substrate preparation

(110)-oriented PMN-PT single crystals (0.25 mm in thickness) with e-beam-deposited Cu(100 nm) top electrode and sputtered Au(100 nm)/Ti(5 nm) bottom electrode are prepoled under an electric field of 6 kV cm⁻¹ across the top and bottom surface. After prepoling, the top surface is first polished using diamond lapping film with 1- μ m grit for 2 min to remove the top Cu electrode and then polished by poromeric polishing pads with a colloidal silica suspension of approximately 60-nm abrasive particles for

15 min to get the average roughness $R_a \sim 0.5$ nm. After polishing, the PMN-PT substrates are annealed at 125 °C for 30 min to set the polarizations in the crystal pointing randomly. We find this step critical to ensure consistent strain responses from PMN-PT under each film force and to preserve the domain configurations against ferroelastic relaxation, which could reorient the polarizations [59,60] underneath the strain gauges after the relief polishing. The R_a after the annealing is below 0.8 nm.

Device fabrication

After the preparation of the PMN-PT substrate, metal thin film strain gauges are patterned using a lift-off process onto the top surface along the [$\bar{1}10$] direction by direct-write laser photolithography using a Microtech LW405 laserwriter system and S1805 photoresist. All metals are deposited using *e*-beam evaporation under a chamber pressure between 1×10^{-5} and 3×10^{-5} torr at a rate of 1 Å s⁻¹. For strain gauges consisting of different metal films, the vacuum condition is maintained throughout the whole deposition process.

Device characterization

Resistance of the strain gauges is measured at room temperature using low frequency ac lock-in techniques (3 Hz) with the ac voltage signal provided by a separated phase-locked function generator. The poling electric fields are applied through gate voltages between the bottom electrode and the strain gauge using a dc power supply and are typically applied for 6 s before each resistance measurement. For all strain gauges, the poling electric fields are cycled between -6 and $+6\,\mathrm{kV}\,\mathrm{cm}^{-1}$ with a step of $0.2\,\mathrm{kV}\,\mathrm{cm}^{-1}$ six times to confirm the repeatability of the results.

Film force characterization

Metal thin films are deposited onto cleaned coverslips using the same evaporation conditions as the fabrication of the strain gauges. The radius of curvature of the coverslips before (r_0) and after (r) the deposition are measured using contact profilometry. The average film stress, $\bar{\sigma}$, is quantified using the Stoney equation [61,62],

$$\bar{\sigma} = \frac{-E_s t_s^2}{6(1 - v_s)t_f} \left(\frac{1}{r} - \frac{1}{r_0}\right),$$

where E_s , v_s , and t_s are the Young's modulus, Poisson's ratio, and the thickness of the coverslip, respectively, and t_f is the thickness of the thin film. The applied film force, F_f , i.e., force per unit width, can then be calculated through $F_f = t_f \bar{\sigma}$.

Strain gauge calibration

The same strain gauges fabricated on the PMN-PT substrates are deposited on flexible Kapton substrates. By applying various amounts of strain through bending the Kapton substrate and measuring the corresponding resistance changes of the strain gauge, the gauge factor is calibrated through the equation $GF = (\Delta R/R)/\varepsilon$, where ε is the applied strain, R is resistance of the strain gauge, and GF is the gauge factor. Here, the value of strain ε is deduced from $\varepsilon = t_k/2r_k$, where $t_k = 127~\mu m$ is the thickness of the Kapton substrate and r_k is the radius of curvature of the bent substrate [16]. The gauge factors for the Ag-only, Ag/Cr bilayer, and Ag/Ni bilayer strain gauge are measured to be 7.7, 7.1, and 5.1, respectively.

Relief polishing

The domains underneath the Ag/Cr bilayer strain gauges are left at the low remanent strain state after the electric-field cycling. The relief polishing process is then conducted as follows. The top surface of the PMN-PT substrate is first polished on a poromeric polishing pad with colloidal silica suspension of approximately 60-nm abrasive particles for 30 s to remove the strain gauges. This is found to be long enough to remove the metal thin film strain gauges while short enough to preserve the domains nanometers below the sample surface, as the abrasion rates of materials with colloidal silica are typically around 40–120 nm min⁻¹ [63]. After that, the surface is polished on another clean poromeric polishing pad with water rinsing turned on for 2 min to clean off the residue polishing media on the PMN-PT surface.

Piezoresponse force microscopy

PFM is performed on an AFM (Solver Next from NT-MDT) using conductive AFM probes (PPP-NCHPt from NANOSENSORS) with a typical voltage of $V_{\rm ac}=1~{\rm V}$ and frequency of 125 kHz between the tip and the bottom electrode of the PMN-PT under ambient conditions at room temperature. To uniquely identify the polarization direction for each domain, VPFM and LPFM are first conducted when the AFM probe is along [001]. After that, the sample is rotated by 90° so that the AFM probe is along [110]. LPFM is then conducted again on the same region. In this way, the components along all three possible Cartesian directions for each polarization are measured.

APPENDIX B: COMPARISON OF INTERFACIAL SHEAR MODULUS OF VARIOUS INTERFACES

Comparison of the interfacial shear modulus $G_{\rm int}$ of similar systems from previously reported studies is listed in Table I. It can be observed that the average interfacial shear modulus varies from as low as about 2 GPa to higher values of about 70 GPa. This value depends on the crystal

TABLE I. Comparison of the interfacial shear modulus of similar metal-dielectric interfaces from the literature.

System	Interfacial shear modulus (GPa)
Ag/PMN-PT (this work)	3.6
Cu/TiN [64]	2.68 ^a
Ti/TiN [65]	3.08 ^a
Ni/Al ₂ O ₃ [66]	5.13 ^a
Ag/MgO [67]	9.35
Al/TiN [64]	12.1 ^a
Ni/ZrO ₂ [68]	31.3
Al/Al_2O_3 [69]	59.6
Al/SiC [70]	70.2

^aCalculated based on the reported values of ideal shear strength and lattice geometry of the system.

structure of the two materials and coherency of the stacked layers. Our system, which has two materials with different crystal structures, experiences some stacking incoherency at the interface. Thus, we obtain a slightly lower value of interfacial shear modulus at the Ag/PMN-PT interface. The deduced $G_{\rm int}$ value from the DFT calculation falls within the range of the interfacial shear modulus values for similar reported systems and hence we use it further for modeling flexoelectric field distribution results in FEA.

APPENDIX C: MODELING DETAILS

DFT simulation of the interfacial shear modulus

We perform DFT simulations to calculate the interfacial shear modulus at the interface of Ag and PMN-PT. All the calculations are performed using the ATOMISTIX TOOLKIT (QuantumATK) commercial package. The selfconsistent calculations are carried out using the Perdew-Burke-Ernzerhof exchange-correlation functional within the generalized gradient approximation [71,72]. The projector augmented wave method [73] is applied with a plane wave cutoff of 400 eV for parametrization of the exchange-correlation functional. An energy convergence criterion of 10⁻⁵ eV is considered for each self-consistent cycle. For simplicity, the PMN-PT crystal has been modeled as having the Pb(Mg_{1/3}Nb_{2/3})O₃ (PMN) structure. Similar to the reports of Suewattana and Singh [74] and Kiguchi et al. [75], the modeled system consists of a 15atom cell with $1 \times 1 \times 3$ superlattice having 1:2 ordering of Mg and Nb. Bulk Ag, which has a face-centered-cubic structure, is stacked on top of the PMN-PT crystal surface. To build the Ag/PMN interface, we stack the PMN and Ag layers in a similar way to that demonstrated by Oleinik et al. [76]. The entire system is relaxed using the conjugate gradient algorithm until the total atomic forces are smaller than cutoff threshold of 0.01 eV $Å^{-1}$. To integrate the Brillouin zone, a $10 \times 10 \times 1$ k-point mesh is used using the Monkhorst-Pack scheme [77]. As in previous works [64,66,67], to obtain the interfacial shear modulus (G_{int}) at the Ag/PMN interface, the Ag layers are displaced over the PMN surface and G_{int} is derived from the interlayer binding energy (E_b) . E_b is obtained as $E_b = E_{Ag/PMN} - E_{Ag} - E_{PMN}$, where $E_{Ag/PMN}$ is the energy of the optimized combined system, and E_{Ag} and E_{PMN} are the energies of the individual optimized Ag and PMN layers. Taking the first order derivative of E_b , we obtain the shear force (F_s) experienced in the sliding direction, and the shear stress, t_t , can be obtained as $t_t = F_s/A$, where A is the area of the Ag/PMN interface. Finally, the interfacial shear modulus is calculated as $G_{\text{int}} = t_t/\varepsilon_t$, where ε_t is the shear strain applied on displacing the Ag layers. In addition, since the Ag layers we deposit are polycrystalline, we consider different orientations of Ag layers by rotating them over the PMN surface and calculating the shear modulus in different directions. We then obtain the average interfacial shear modulus (3.6 GPa) by incorporating all considered orientations.

FEA simulation of the strain distribution

To model the strain gradient and the resultant flexoelectric field distributions in the PMN-PT under the application of stress from the metal thin films, FEA is conducted using ABAQUS, a commercially available program. The metal films and PMN-PT substrates are modeled in a plane strain condition (as the length of the metal strip is approximately 50 times larger than the width in our fabricated devices) with eight-node quadratic plane strain (CPE8) elements. All the materials are taken to be isotropic and linearly elastic with Young's modulus of 279, 83, and 20 GPa [78,79] and Poisson's ratio of 0.21, 0.37, and 0.3 for Cr, Ag, and PMN-PT, respectively. The width of both metal films is set to 10 μ m with their thicknesses taken to be 50 nm and 25 nm, respectively, for the Cr and Ag layer. The PMN-PT substrate is 30 μ m wide with a thickness of 10 μ m. A fine mesh size of 20 nm is created in the substrate, which results in a total of 750 000 elements to provide a fine resolution for calculations of strain gradients. In addition, dimensions and mesh size are selected such that the strain field underneath the metal-substrate interface reaches convergence and is unaffected by the geometry of the edges.

The behavior of the Ag/PMN-PT interface is described by a cohesive zone model (CZM) with a linear traction-separation law already implemented in ABAQUS. In this way, the interface can be made relatively compliant (lower stiffness) than the two constituting elastic bodies as observed from the DFT simulations. The traction-separation law can be surface based in ABAQUS where the stiffness is defined as an interaction property, or element based where it is defined as a material property, although the constitutive relations are almost the same for both descriptions. The constitutive relationship for 2D cohesive

elements can be written as follows [80]:

$$\mathbf{T} = \begin{pmatrix} t_n \\ t_t \end{pmatrix} = \begin{bmatrix} k_{nn} & k_{nt} \\ k_{nt} & k_{tt} \end{bmatrix} \begin{pmatrix} \varepsilon_n \\ \varepsilon_t \end{pmatrix} = \mathbf{K}\boldsymbol{\varepsilon}$$
 (C1)

where t_n and t_t are the traction stress components in the normal and shear direction, respectively, **K** is the nominal cohesive stiffness matrix of the interface, and ε_n and ε_t are the corresponding nominal strain components. For the uncoupled linear traction-separation behavior (ε_t does not give rise to stress in the normal direction and vice versa), the off-diagonal terms can be set to zero and the constitutive response then becomes

$$\mathbf{T} = \begin{pmatrix} t_n \\ t_t \end{pmatrix} = \begin{bmatrix} k_{nn} & 0 \\ 0 & k_{tt} \end{bmatrix} \begin{pmatrix} \varepsilon_n \\ \varepsilon_t \end{pmatrix} = \mathbf{K}\boldsymbol{\varepsilon}. \tag{C2}$$

We set the stiffness matrix element k_{tt} in Eq. (C2) equal to G_{int} from our DFT calculation. Now, the nominal strains in Eq. (C2) are defined as follows: $\varepsilon_n = \delta_n/T_o$, $\varepsilon_t = \delta_t/T_o$, where δ_n is the normal separation (debonding) and δ_t is the shear separation (slippage) across the interface, T_o is the constitutive thickness of the cohesive element. If the value of T_o is taken to be 1.0, then the nominal strains in Eq. (C2) become equal to the corresponding separations. As a result, the constitutive relationship can be equivalently written as

$$\mathbf{T} = \begin{pmatrix} t_n \\ t_t \end{pmatrix} = \begin{bmatrix} k_{nn} & 0 \\ 0 & k_{tt} \end{bmatrix} \begin{pmatrix} \delta_n \\ \delta_t \end{pmatrix} = \mathbf{K}\boldsymbol{\delta}, \quad (C3)$$

which is the traction-separation constitutive law for a surface-based cohesive model in ABAQUS. In this work, we use the surface-based linear elastic CZM along with the assumption that no damage occurs at the interface.

As the applied tensile film stress is expected to transfer from the metal to substrate by interfacial shear stress, and no normal debonding is observed, only the shear tractionseparation law is assumed in the cohesive model, i.e., $k_{nn} = 0$ in Eq. (C3). In the surface-based cohesive model, interface slippage δ_t is defined as the contact separation, which is the relative displacement between the nodes on one surface (PMN-PT) and their corresponding projection points on the other contacting surface (Ag) along the contact (interface) shear direction. Concepts of strain and displacement are reinterpreted as contact separations as mentioned earlier. The cohesive model represents the interface by an equivalent spring connecting the two elastic bodies (metal film and PMN-PT). A similar cohesive law has been used previously for describing many different types of interfaces [81–84].

We set the magnitude of the shear stiffness parameter in the FEA model to be the same as the average G_{int} obtained from our DFT simulations. Furthermore, the choice of

this model parameter best reproduces experimental observations. A comparison with the results from stiffer (no slippage) as well as more compliant (smaller $G_{\rm int}$, strong slippage) interfaces that may be possible from different relative orientations of two crystals are also presented as an additional validation in Appendix D (Fig. 6). Biaxial tensile stresses of 966 and 60 MPa (taken from experimental measurements) are applied on the Cr and Ag films, respectively, with a fixed boundary condition imposed at the bottom of the PMN-PT along the thickness direction while keeping its edges free. Both normal and shear strain components at every elemental node are used from the FEA models to numerically calculate the corresponding strain gradients.

Calculation of flexoelectric field

Flexoelectric polarization is given by $P_l = \mu_{ijkl} \frac{\partial \epsilon_{kl}}{\partial x_j}$ [28,29], where μ_{ijkl} is the flexoelectric tensor, ε_{kl} is the strain, and x_i is the spatial coordinate. For PMN-PT with rhombohedral symmetry, μ_{ijkl} has 18 independent components [85]. However, full flexoelectric tensor components for PMN-PT have never been calculated theoretically and extracting all coefficients from experiment is challenging. In fact, only the effective transverse flexoelectric coefficient μ_{13}^{eff} for (100)-oriented PMN-PT has been measured experimentally, with a value in the range 10–70 μ C cm⁻¹ at room temperature [41,42]. To make an estimation of each tensor component, we assume cubic symmetry of PMN-PT and take $\mu_{1111} = \mu_{2222} = \mu_{3333} = \mu_{11} =$ 1 μ C cm⁻¹, $\mu_{1122} = \mu_{1133} = \mu_{2211} = \mu_{2233} = \mu_{3311} = \mu_{3322} = \mu_{12} = 16 \,\mu$ C cm⁻¹, and $\mu_{1221} = \mu_{1331} = \mu_{2112} = \mu_{2332} = \mu_{3112} = \mu_{3223} = \mu_{44} = 1 \,\mu$ C cm⁻¹ for (100)-oriented PMN-PT. Based on the equation, $\mu_{13}^{\text{eff}} = [-c_{12}/(c_{11} + c_{12})]\mu_{11} +$ $[c_{11}/(c_{11}+c_{12})]\mu_{12}$ [86,87], where c_{11} and c_{12} are the elastic stiffness tensor components of PMN-PT [78], the estimated tensor values yield an effective transverse flexoelectric coefficient of around 10 μ C cm⁻¹, which is within the range of the experimental value. For (110)oriented PMN-PT, as the coordinates are rotated from where \hat{x}_1 , \hat{x}_2 , and \hat{x}_3 are along [001], [010], and [100], respectively, to along [110], [001], and [110], respectively, the flexoelectric coefficients therefore transform to $\mu'_{33} = (\mu_{11} + \mu_{12} + 2\mu_{44})/2 = 9.5 \ \mu\text{C cm}^{-1}, \ \mu'_{22} = \mu_{11} = 1 \ \mu\text{C cm}^{-1}, \ \mu'_{23} = \mu'_{32} = \mu_{12} = 16 \ \mu\text{C cm}^{-1}, \ \mu'_{44} = \mu_{44} = 1 \ \mu\text{C cm}^{-1}$ [86]. Under the assumption of plane strain, only strains ε_{22} , ε_{33} , and ε_{23} are considered. Flexoelectric polarization, $\vec{P}(0, P_2, P_3)$, can, therefore, be calculated by $P_2 = \mu'_{22} \frac{\partial \varepsilon_{22}}{\partial x_2} + \mu'_{23} \frac{\partial \varepsilon_{33}}{\partial x_2} + \mu'_{44} \frac{\partial \varepsilon_{23}}{\partial x_3}$, $P_3 = \mu'_{33} \frac{\partial \varepsilon_{33}}{\partial x_3} + \mu'_{32} \frac{\partial \varepsilon_{22}}{\partial x_3} + \mu'_{44} \frac{\partial \varepsilon_{23}}{\partial x_2}$ [88], where the strain gradients are obtained from the FEA model. Flexoelectric field, E_{flexo} , is derived from the flexoelectric polarization by $\vec{E}_{\text{flexo}} = \vec{P}/\varepsilon_0 \varepsilon_r$, where ε_0 is the permittivity of a vacuum and $\varepsilon_r = 1800$ for PMN-PT [78].

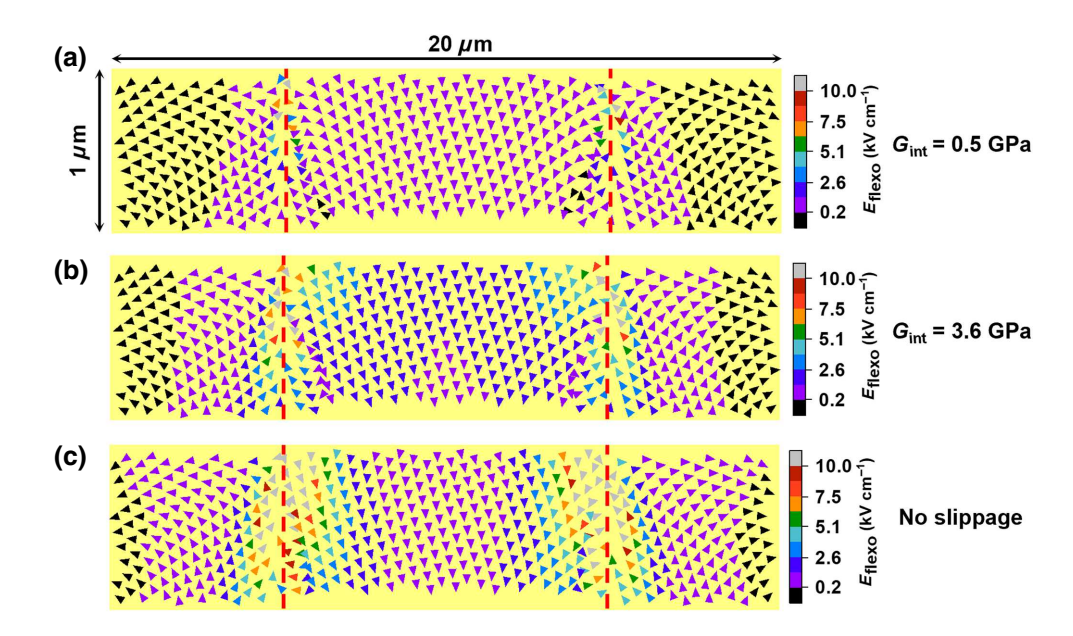


FIG. 6. (a)—(c) Calculated flexoelectric field ($E_{\rm flexo}$) distribution inside the PMN-PT underneath the Ag/Cr bilayer film based on the assumption of $G_{\rm int}$ = 0.5 GPa, 3.6 GPa, and no slippage, respectively. Here, the direction and the color of each arrow represent the direction and the magnitude of $E_{\rm flexo}$, respectively. The red dashed lines show where the edges of the Ag/Cr bilayer film are located.

APPENDIX D: COMPARISON OF THE SIMULATED FLEXOELECTRIC FIELD BASED ON DIFFERENT VALUES OF $G_{\rm inf}$

Simulated flexoelectric fields inside the PMN-PT underneath the Ag/Cr bilayer film based on different values of $G_{\rm int}$ are shown in Fig. 6, where $G_{\rm int}$ increases from a strong slippage condition ($G_{\rm int}=0.5$ GPa) to the no slippage condition. As shown in Fig. 6, when the value of $G_{\rm int}$ is at 3.6 GPa, the magnitude of $E_{\rm flexo}$ near the surface of the PMN-PT underneath the strip is above 2 kV cm⁻¹, whereas in both the strong slippage and the no slippage conditions, the magnitude of $E_{\rm flexo}$ near the surface of the PMN-PT underneath the strip decreases to below half of the coercive field of PMN-PT (<0.8 kV cm⁻¹).

- [1] J. F. Scott and C. A. P. Dearaujo, Ferroelectric memories, Science **246**, 1400 (1989).
- [2] S. Mathews, R. Ramesh, T. Venkatesan, and J. Benedetto, Ferroelectric field effect transistor based on epitaxial perovskite heterostructures, Science **276**, 238 (1997).
- [3] P. Maksymovych, S. Jesse, P. Yu, R. Ramesh, A. P. Baddorf, and S. V. Kalinin, Polarization control of electron tunneling into ferroelectric surfaces, Science 324, 1421 (2009).
- [4] V. Garcia, S. Fusil, K. Bouzehouane, S. Enouz-Vedrenne, N. D. Mathur, A. Barthelemy, and M. Bibes, Giant tunnel electroresistance for non-destructive readout of ferroelectric states, Nature 460, 81 (2009).
- [5] G. Arlt and H. Neumann, Internal bias in ferroelectric ceramics: Origin and time dependence, Ferroelectrics 87, 109 (1988).
- [6] S. Wu, S. A. Cybart, D. Yi, J. M. Parker, R. Ramesh, and R. Dynes, Full Electric Control of Exchange Bias, Phys. Rev. Lett. 110, 067202 (2013).

- [7] S. Wu, S. A. Cybart, P. Yu, M. Rossell, J. Zhang, R. Ramesh, and R. Dynes, Reversible electric control of exchange bias in a multiferroic field-effect device, Nat. Mater. 9, 756 (2010).
- [8] A. R. Damodaran, E. Breckenfeld, Z. H. Chen, S. Lee, and L. W. Martin, Enhancement of ferroelectric curie temperature in BaTiO₃ films via strain-induced defect dipole alignment, Adv. Mater. 26, 6341 (2014).
- [9] S. Saremi, J. Kim, A. Ghosh, D. Meyers, and L. W. Martin, Defect-Induced (Dis)Order in Relaxor Ferroelectric Thin Films, Phys. Rev. Lett. 123, 207602 (2019).
- [10] D. Lee, B. C. Jeon, A. Yoon, Y. J. Shin, M. H. Lee, T. K. Song, S. D. Bu, M. Kim, J. S. Chung, J. G. Yoon, *et al.*, Flexoelectric control of defect formation in ferroelectric epitaxial thin films, Adv. Mater. 26, 5005 (2014).
- [11] P. Yu, W. Luo, D. Yi, J. X. Zhang, M. D. Rossell, C. H. Yang, L. You, G. Singh-Bhalla, S. Y. Yang, Q. He, et al., Interface control of bulk ferroelectric polarization, Proc. Natl. Acad. Sci. U. S. A. 109, 9710 (2012).
- [12] C. Lichtensteiger, S. Fernandez-Pena, C. Weymann, P. Zubko, and J. M. Triscone, Tuning of the depolarization field and nanodomain structure in ferroelectric thin films, Nano Lett. 14, 4205 (2014).
- [13] B. C. Jeon, D. Lee, M. H. Lee, S. M. Yang, S. C. Chae, T. K. Song, S. D. Bu, J. S. Chung, J. G. Yoon, and T. W. Noh, Flexoelectric effect in the reversal of self-polarization and associated changes in the electronic functional properties of BiFeO₃ thin films, Adv. Mater. 25, 5643 (2013).
- [14] D. Lee, A. Yoon, S. Jang, J.-G. Yoon, J.-S. Chung, M. Kim, J. Scott, and T. W. Noh, Giant Flexoelectric Effect in Ferroelectric Epitaxial Thin Films, Phys. Rev. Lett. 107, 057602 (2011).
- [15] A. M. Smith, A. M. Mohs, and S. Nie, Tuning the optical and electronic properties of colloidal nanocrystals by lattice strain, Nat. Nanotechnol. 4, 56 (2009).
- [16] O. B. Aslan, I. M. Datye, M. J. Mleczko, K. Sze Cheung, S. Krylyuk, A. Bruma, I. Kalish, A. V. Davydov, E. Pop, and T. F. Heinz, Probing the optical properties and

- strain-tuning of ultrathin $Mo_{1-x}W_xTe_2$, Nano Lett. **18**, 2485 (2018).
- [17] R. Cherifi, V. Ivanovskaya, L. Phillips, A. Zobelli, I. Infante, E. Jacquet, V. Garcia, S. Fusil, P. Briddon, and N. Guiblin, Electric-field control of magnetic order above room temperature, Nat. Mater. 13, 345 (2014).
- [18] Y. Lee, Z. Liu, J. T. Heron, J. D. Clarkson, J. Hong, C. Ko, M. D. Biegalski, U. Aschauer, S.-L. Hsu, and M. E. Nowakowski, Large resistivity modulation in mixed-phase metallic systems, Nat. Commun. 6, 5959 (2015).
- [19] S. Zhang, Y. G. Zhao, P. S. Li, J. J. Yang, S. Rizwan, J. X. Zhang, J. Seidel, T. L. Qu, Y. J. Yang, Z. L. Luo, et al., Electric-Field Control of Nonvolatile Magnetization in Co₄₀Fe₄₀B₂₀/Pb(Mg_{1/3}Nb_{2/3})_{0.7}Ti_{0.3}O₃ Structure at Room Temperature, Phys. Rev. Lett. 108, 137203 (2012).
- [20] W. Zhou, C. Ma, Z. Gan, Z. Zhang, X. Wang, W. Tan, and D. Wang, Manipulation of anisotropic magnetoresistance and domain configuration in Co/PMN-PT (011) multiferroic heterostructures by electric field, Appl. Phys. Lett. 111, 052401 (2017).
- [21] M. Liu, J. Hoffman, J. Wang, J. Zhang, B. Nelson-Cheeseman, and A. Bhattacharya, Non-volatile ferroe-lastic switching of the verwey transition and resistivity of epitaxial Fe₃O₄/PMN-PT (011), Sci. Rep. 3, 1876 (2013).
- [22] M. Liu, B. M. Howe, L. Grazulis, K. Mahalingam, T. X. Nan, N. X. Sun, and G. J. Brown, Voltage-Impulse-Induced Non-volatile ferroelastic switching of ferromagnetic resonance for reconfigurable magnetoelectric microwave devices, Adv. Mater. 25, 4886 (2013).
- [23] W. Hou, A. Azizimanesh, A. Sewaket, T. Pena, C. Watson, M. Liu, H. Askari, and S. M. Wu, Strain-based roomtemperature non-volatile MoTe₂ ferroelectric phase change transistor, Nat. Nanotechnol. 14, 668 (2019).
- [24] A. Chen, A review of emerging non-volatile memory (NVM) technologies and applications, Solid-State Electron. 125, 25 (2016).
- [25] T. Wu, P. Zhao, M. Bao, A. Bur, J. L. Hockel, K. Wong, K. P. Mohanchandra, C. S. Lynch, and G. P. Carman, Domain engineered switchable strain states in ferroelectric $(011)[Pb(Mg_{1/3}Nb_{2/3})O_3]_{(1-x)}$ -[PbTiO₃]_x (PMN-PT, $x\approx0.32$) single crystals, J. Appl. Phys. **109**, 124101 (2011).
- [26] D. Lupascu and J. Rödel, Fatigue in bulk lead zirconate titanate actuator materials, Adv. Eng. Mater. 7, 882 (2005).
- [27] W. H. Liang, F. X. Hu, J. Zhang, H. Kuang, J. Li, J. F. Xiong, K. M. Qiao, J. Wang, J. R. Sun, and B. G. Shen, Anisotropic nonvolatile magnetization controlled by electric field in amorphous SmCo thin films grown on (011)-cut PMN-PT substrates, Nanoscale 11, 246 (2019).
- [28] P. Zubko, G. Catalan, and A. K. Tagantsev, Flexoelectric effect in solids, Annu. Rev. Mater. Res. 43, 387 (2013).
- [29] B. Wang, Y. Gu, S. Zhang, and L.-Q. Chen, Flexoelectricity in solids: Progress, challenges, and perspectives, Prog. Mater. Sci. 106, 100570 (2019).
- [30] G. Tsutsui, S. Mochizuki, N. Loubet, S. W. Bedell, and D. K. Sadana, Strain engineering in functional materials, AIP Adv. 9, 030701 (2019).
- [31] T. Acosta and S. Sood, Engineering strained silicon-looking back and into the future, IEEE Potentials 25, 31 (2006).
- [32] S. E. Thompson, G. Sun, Y. S. Choi, and T. Nishida, Uniaxial-process-induced strained-Si: Extending the

- CMOS roadmap, IEEE Trans. Electron Devices **53**, 1010 (2006).
- [33] S. Orain, V. Fiori, D. Villanueva, A. Dray, and C. Ortolland, Method for managing the stress due to the strained nitride capping layer in MOS transistors, IEEE Trans. Electron Devices **54**, 814 (2007).
- [34] G. Catalan, A. Lubk, A. Vlooswijk, E. Snoeck, C. Magen, A. Janssens, G. Rispens, G. Rijnders, D. H. Blank, and B. Noheda, Flexoelectric rotation of polarization in ferroelectric thin films, Nat. Mater. 10, 963 (2011).
- [35] H. Lu, C.-W. Bark, D. E. De Los Ojos, J. Alcala, C. B. Eom, G. Catalan, and A. Gruverman, Mechanical writing of ferroelectric polarization, Science 336, 59 (2012).
- [36] J. Ocenasek, H. Lu, C. W. Bark, C. B. Eom, J. Alcala, G. Catalan, and A. Gruverman, Nanomechanics of flexoelectric switching, Phys. Rev. B 92, 035417 (2015).
- [37] K. Cordero-Edwards, N. Domingo, A. Abdollahi, J. Sort, and G. Catalan, Ferroelectrics as smart mechanical materials, Adv. Mater. 29, 1702210 (2017).
- [38] S. M. Park, B. Wang, S. Das, S. C. Chae, J. S. Chung, J. G. Yoon, L. Q. Chen, S. M. Yang, and T. W. Noh, Selective control of multiple ferroelectric switching pathways using a trailing flexoelectric field, Nat. Nanotechnol. 13, 366 (2018).
- [39] S. S. Cheema, D. Kwon, N. Shanker, R. dos Reis, S. L. Hsu, J. Xiao, H. G. Zhang, R. Wagner, A. Datar, M. R. McCarter, *et al.*, Enhanced ferroelectricity in ultrathin films grown directly on silicon, Nature 580, 478 (2020).
- [40] A. I. Khan, A. Keshavarzi, and S. Datta, The future of ferroelectric field-effect transistor technology, Nat. Electron. 3, 588 (2020).
- [41] J. Narvaez and G. Catalan, Origin of the enhanced flexoelectricity of relaxor ferroelectrics, Appl. Phys. Lett. 104, 162903 (2014).
- [42] L. Shu, M. Wan, X. Jiang, F. Li, N. Zhou, W. Huang, and T. Wang, Frequency dispersion of flexoelectricity in PMN-PT single crystal, AIP Adv. 7, 015010 (2017).
- [43] R. Koch, Stress in evaporated and sputtered thin films—a comparison, Surf. Coat. Technol. 204, 1973 (2010).
- [44] R. Abermann and R. Koch, The internal stress in thin silver, copper and gold films, Thin Solid Films 129, 71 (1985).
- [45] L. M. Zheng, L. Y. Yang, Y. R. Li, X. Y. Lu, D. Huo, W. M. Lu, R. Zhang, B. Yang, and W. W. Cao, Origin of Improvement in Mechanical Quality Factor in Acceptor-Doped Relaxor-Based Ferroelectric Single Crystals, Phys. Rev. Appl. 9, 064028 (2018).
- [46] C. He, Z. J. Wang, X. Z. Li, X. M. Yang, X. F. Long, and Z. G. Ye, Self-polarized high piezoelectricity and its memory effect in ferroelectric single crystals, Acta Mater. 125, 498 (2017).
- [47] M. Stengel, D. Vanderbilt, and N. A. Spaldin, Enhancement of ferroelectricity at metal-oxide interfaces, Nat. Mater. 8, 392 (2009).
- [48] E. Klokholm and B. Berry, Intrinsic stress in evaporated metal films, J. Electrochem. Soc. 115, 823 (1968).
- [49] F. Johann, Y. J. Ying, T. Jungk, A Hoffmann, C. L. Sones, R. W. Eason, S. Mailis, and E. Soergel, Depth resolution of piezoresponse force microscopy, Appl. Phys. Lett. 94, 172904 (2009).
- [50] M. F. Wong and K. Zeng, Mechanical polishing effects toward surface domain evolution in Pb(Zn_{1/3}Nb_{2/3})O₃—

- PbTiO₃ single crystals, J. Am. Ceram. Soc. **94**, 1079 (2011).
- [51] A. R. Akhmatkhanov, E. D. Greshnyakov, A. D. Ushakov, E. M. Vaskina, D. O. Alikin, X. Wei, Z. Xu, Z. Li, S. Wang, Y. Zhuang, et al., Polarization reversal and domain kinetics in PMN-30PT single crystals, Ferroelectrics 508, 31 (2017).
- [52] Q. Hu, A. D. Ushakov, A. A. Esin, E. O. Vlasov, D. S. Chezganov, L. Sun, A. P. Turygin, X. Wei, and V. Y. Shur, Investigation of domain structure evolution during zero-field temperature treatment in 0.67PMN-0.33PT single crystals, Ferroelectrics 525, 114 (2018).
- [53] T. Scholz, B. Mihailova, G. A. Schneider, N. Pagels, J. Heck, T. Malcherek, R. P. Fernandes, V. Marinova, M. Gospodinov, and U. Bismayer, Ferroelectric properties of ruthenium-doped lead zinc niobate-lead titanate single crystal, J. Appl. Phys. 106, 074108 (2009).
- [54] Q. Li, Y. Liu, R. L. Withers, Y. H. Wan, Z. R. Li, and Z. Xu, Piezoresponse force microscopy studies on the domain structures and local switching behavior of Pb(In_{1/2}Nb_{1/2})O₃-Pb(Mg_{1/3}Nb_{2/3})O₃-PbTiO₃ single crystals, J. Appl. Phys. **112**, 052006 (2012).
- [55] A. Gruverman, B. J. Rodriguez, A. I. Kingon, R. J. Nemanich, A. K. Tagantsev, J. S. Cross, and M. Tsukada, Mechanical stress effect on imprint behavior of integrated ferroelectric capacitors, Appl. Phys. Lett. 83, 728 (2003)
- [56] G. H. Dong, S. Z. Li, M. T. Yao, Z. Y. Zhou, Y. Q. Zhang, X. Han, Z. L. Luo, J. X. Yao, B. Peng, Z. Q. Hu, et al., Super-elastic ferroelectric single-crystal membrane with continuous electric dipole rotation, Science 366, 475 (2019).
- [57] J. Irwin, S. Lindemann, W. Maeng, J. J. Wang, V. Vaithyanathan, J. M. Hu, L. Q. Chen, D. G. Schlom, C. B. Eom, and M. S. Rzchowski, Magnetoelectric coupling by piezoelectric tensor design, Sci. Rep. 9, 19158 (2019).
- [58] H. S. Kum, H. Lee, S. Kim, S. Lindemann, W. Kong, K. Qiao, P. Chen, J. Irwin, J. H. Lee, S. E. Xie, *et al.*, Heterogeneous integration of single-crystalline complex-oxide membranes, Nature 578, 75 (2020).
- [59] M. P. Cruz, Y. H. Chu, J. X. Zhang, P. L. Yang, F. Zavaliche, Q. He, P. Shafer, L. Q. Chen, and R. Ramesh, Strain Control of Domain-Wall Stability in Epitaxial BiFeO₃ (110) Films, Phys. Rev. Lett. 99, 217601 (2007).
- [60] S. H. Baek, H. W. Jang, C. M. Folkman, Y. L. Li, B. Winchester, J. X. Zhang, Q. He, Y. H. Chu, C. T. Nelson, M. S. Rzchowski, *et al.*, Ferroelastic switching for nanoscale non-volatile magnetoelectric devices, Nat. Mater. 9, 309 (2010).
- [61] J. S. Kim, K. W. Paik, and S. H. Oh, The multilayer-modified stoney's formula for laminated polymer composites on a silicon substrate, J. Appl. Phys. 86, 5474 (1999).
- [62] G. C. Janssen, M. Abdalla, F. Van Keulen, B. Pujada, and B. Van Venrooy, Celebrating the 100th anniversary of the stoney equation for film stress: Developments from polycrystalline steel strips to single crystal silicon wafers, Thin Solid Films 517, 1858 (2009).
- [63] Z. Zhang, W. Liu, and Z. Song, Effect of ammonium molybdate concentration on chemical mechanical polishing of glass substrate, J. Semicond. **31**, 116003 (2010).

- [64] S. K. Yadav, R. Ramprasad, J. Wang, A. Misra, and X. Y. Liu, First-principles study of Cu/TiN and Al/TiN interfaces: Weak versus strong interfaces, Model. Simul. Mater. Sci. Eng. 22, 035020 (2014).
- [65] X. M. Zhang, B. Zhang, Y. Mu, S. Shao, C. D. Wick, B. R. Ramachandran, and W. J. Meng, Mechanical failure of metal/ceramic interfacial regions under shear loading, Acta Mater. 138, 224 (2017).
- [66] X. C. Guo and F. L. Shang, Shear strength and sliding behavior of Ni/Al₂O₃ interfaces: A first-principle study, J. Mater. Res. 27, 1237 (2012).
- [67] X. Q. Fu, L. H. Liang, and Y. G. Wei, Atomistic simulation study on the shear behavior of Ag/MgO interface, Comput. Mater. Sci. 155, 116 (2018).
- [68] X. Y. Guo, Y. Zhang, Y. G. Jung, L. Li, J. Knapp, and J. Zhang, Ideal tensile strength and shear strength of ZrO₂(111)/Ni(111) ceramic-metal interface: A first principle study, Mater. Des. 112, 254 (2016).
- [69] A. Sazgar, M. R. Movahhedy, M. Mahnama, and S. Sohrabpour, A molecular dynamics study of bond strength and interface conditions in the Al/Al₂O₃ metal-ceramic composites, Comput. Mater. Sci. 109, 200 (2015).
- [70] C. R. Dandekar and Y. C. Shin, Molecular dynamics based cohesive zone law for describing Al-SiC interface mechanics, Composites, Part A 42, 355 (2011).
- [71] A. Dey, B. A. Baraiya, S. Adhikary, and P. K. Jha, First-Principles calculations of the effects of edge functionalization and size on the band Gap of Be₃N₂ nanoribbons: Implications for nanoelectronic devices, ACS Appl. Nano Mater. **4**, 493 (2021).
- [72] J. P. Perdew, K. Burke, and M. Ernzerhof, Generalized Gradient Approximation Made Simple, Phys. Rev. Lett. 77, 3865 (1996).
- [73] P. E. Blochl, Projector augmented-wave method, Phys. Rev. B 50, 17953 (1994).
- [74] M. Suewattana and D. J. Singh, Electronic structure and lattice distortions in PbMg_{1/3}Nb_{2/3}O₃ studied with density functional theory using the linearized augmented planewave method, Phys. Rev. B **73**, 224105 (2006).
- [75] T. Kiguchi, N. Wakiya, K. Shinozaki, and T. J. Konno, Valence-EELS analysis of local electronic and optical properties of PMN-PT epitaxial film, Mater. Sci. Eng., B 161, 160 (2009).
- [76] I. I. Oleinik, E. Y. Tsymbal, and D. G. Pettifor, Atomic and electronic structure of Co/SrTiO₃/Co magnetic tunnel junctions, Phys. Rev. B 65, 020401(R) (2002).
- [77] H. J. Monkhorst and J. D. Pack, Special points for brillouinzone integrations, Phys. Rev. B 13, 5188 (1976).
- [78] J. Kim, C. Joh, and Y. Roh, Evaluation of All the material constants of PMN-28% PT piezoelectric single crystals for acoustic transducers, Sens. Mater. **25**, 539 (2013).
- [79] L. M. Ewart, E. A. Mclaughlin, H. C. Robinson, J. J. Stace, and A. Amin, Mechanical and electromechanical properties of PMNT single crystals for naval sonar transducers, IEEE Trans. Ultrason. Ferroelectr. Freq. Control 54, 2469 (2007).
- [80] ABAQUS Version 6.11 Documentation Collection (Dassault Systèmes Simulia Corp., Providence, RI, USA, 2011).
- [81] L. Y. Jiang, Y. Huang, H. Jiang, G. Ravichandran, H. Gao, K. C. Hwang, and B. Liu, A cohesive law for carbon

- nanotube/polymer interfaces based on the van der waals force, J. Mech. Phys. Solids **54**, 2436 (2006).
- [82] G. D. Guo and Y. Zhu, Cohesive-Shear-Lag modeling of interfacial stress transfer between a monolayer graphene and a polymer substrate, J. Appl.Mech. 82, 031005 (2015).
- [83] M. Safaei, A. Sheidaei, M. Baniassadi, S. Ahzi, M. M. Mashhadi, and F. Pourboghrat, An interfacial debonding-induced damage model for graphite nanoplatelet polymer composites, Comput. Mater. Sci. 96, 191 (2015).
- [84] S. A. Chowdhury and H. Askari, A unified model for the effective elastic response of inhomogeneities with finite sliding, Int. J. Mech. Sci. 153, 470 (2019).
- [85] L. L. Shu, X. Y. Wei, T. Pang, X. Yao, and C. L. Wang, Symmetry of flexoelectric coefficients in crystalline medium, J. Appl. Phys. 110, 104106 (2011).
- [86] J. Narvaez, S. Saremi, J. W. Hong, M. Stengel, and G. Catalan, Large Flexoelectric Anisotropy in Paraelectric Barium Titanate, Phys. Rev. Lett. **115**, 037601 (2015).
- [87] P. Zubko, G. Catalan, A. Buckley, P. R. L. Welche, and J. F. Scott, Strain-Gradient-Induced Polarization in SrTiO₃ Single Crystals, Phys. Rev. Lett. 99, 167601 (2007).
- [88] W. H. Ma, A study of flexoelectric coupling associated internal electric field and stress in thin film ferroelectrics, Phys. Status Solidi B **245**, 761 (2008).